ACS NANO

ARTICLE

Nanosizing a Metal−Organic Framework Enzyme Carrier for Accelerating Nerve Agent Hydrolysis

Peng Li,[†] Su-Young Moon,[†] Mark A. Guelta,[§] Lu Lin,[†,‖] Diego A. Gómez-Gualdrón,[‡] Randall Q. Snurr,[‡] Steven P. Harvey,[§] Joseph T. Hupp,[†] and Omar K. Farha*,[†,⊥]

[†]Department of Chemistry and [‡]Department of Chemical and Biological Engineering, Northwestern University, 2145 Sheridan Road, Evanston, Illinois 60208, United States

[§]U.S. Army Edgewood Chemical Biological Center, 5183 Blackhawk Road, RDCB-DRC-C, Aberdeen Proving Ground, Maryland 21010-5424, United States

[‖]State Key Laboratory of Fine Chemicals, School of Chemical Engineering, Dalian University of Technology, Dalian 116024, People's Republic of China

[⊥]Department of Chemistry, Faculty of Science, King Abdulaziz University, Jeddah 21589, Saudi Arabia

S *Supporting Information*

ABSTRACT: We report the synthesis and characterization of a water-stable zirconium metal−organic framework (MOF), NU-1003, featuring the largest mesoporous aperture known for a zirconium MOF. This material has been used to immobilize the nerve agent hydrolyzing enzyme, organophosphorus acid anhydrolase (OPAA). The catalytic efficiency of immobilized OPAA in *nanosized* NU-1003 is significantly increased compared to that of OPAA immobilized in *microsized* NU-1003 and even exceeds that of the free OPAA enzyme. This paper highlights a method for rapid and highly efficient hydrolysis of nerve agents using nanosized enzyme carriers.

KEYWORDS: metal−organic framework, enzyme immobilization, nerve agent catalysis, nanocarrier
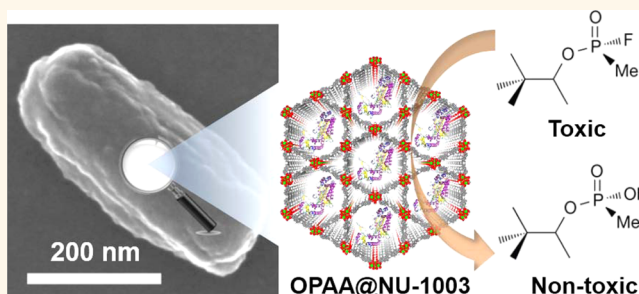
Nerve agents are highly toxic chemical weapons that can cause death after only a very short exposure time.[1−3] As a complementary and synergetic approach to current antidotal treatments, the use of catalytic enzymes,[4−6] such as organophosphorus acid anhydrolase (OPAA),[7] to hydrolyze nerve agents in the blood has received broad interest. However, free enzyme is cleared rapidly by the immune system, and while it might provide postexposure protection, it is unlikely to protect in a prophylactic manner due to the clearance rates.[8,9] Previously, biodegradable liposome nanocarriers have been shown to be effective at providing functionally significant amounts of highly purified enzymes in the bloodstream while protecting the enzymes for over 2 days.[10] Highly desirable, nevertheless, are approaches that may yield comparably high activity and stability, while providing ancillary benefits such as simpler handling and storage of enzymes.[11]

Metal−organic frameworks (MOFs),[12] consisting of metal ions/clusters and coordinated organic linkers, represent a class of highly crystalline porous materials with regular crystal morphology, adjustable pore diameters, and tunable function-alities. MOFs have been studied for applications in, but not limited to, storage and release,[13,14] sensing,[15−17] and separation[18,19] of small ions,[20,21] gases,[22] and large organic[23−25] and inorganic molecules, among others.[26,27] Recent advances in the development of water-stable mesoporous MOFs[28] have allowed for their use as enzyme carriers[11,29−37] to stabilize enzymes in challenging conditions such as organic solvent,[35,38] elevated temperature, and over long-term storage.[11] As a result of their highly crystalline and porous nature,[12] MOFs tend to show higher loading capacities and stronger interactions with guest enzymes (leading to less leaching) compared to other porous materials such as mesoporous silica (MPS).[35] Previously, we have systematically investigated the diffusion, spatial distribution, and accessibility of an enzyme encapsulated in a series of channel-type MOFs[38] and demonstrated that a *csq-net* zirconium-based MOF,[39−42] composed of interconnected

hierarchical hexagonal mesoporous and triangular microporous channels, is superior to other existing channel-type MOFs for this application.[43,44]

Although most known MOF−enzyme systems have been shown to protect the immobilized enzymes from deactivation, the initial catalytic turnover rates of immobilized enzymes are often much lower than those of free enzymes in solution.[11,29,35] This is attributed to a diffusion barrier that must be overcome for reactants to access enzymes sited in the interior of MOF crystals.[45] In order to react with (*i.e.*, fully utilize) all encapsulated enzymes, reactants must diffuse throughout the entire MOF−enzyme crystal. Typically, when micron-sized porous crystals are used, however, the concentration of reactants at the pore opening and on the MOF surface is higher than that at the interior of the crystal. As a result, the enzymes immobilized in the interior of a micron-sized MOF crystal are not as accessible (Scheme 1), and therefore, the rate

Scheme 1. Schematic Representation of a MOF−Enzyme Carrier with Evenly Immobilized Enzymes (Orange Circles) and Diffusion of Reactant Molecules (Green Circles) from Solution into the MOF−Enzyme Carrier
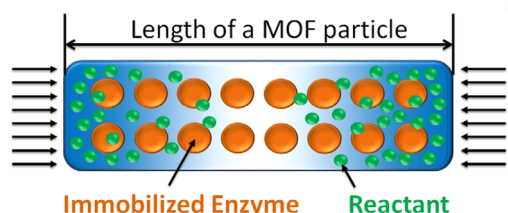
of reaction throughout the MOF−enzyme carrier will vary. This will result in an overall reaction rate lower than that at the external surface of the MOF−enzyme carrier. Theoretically, this internal diffusion and reaction limitation can be minimized by enlarging the aperture of the cavity and/or minimizing the size of the MOF−enzyme crystals into the nanoregime.[46]

Various approaches have been developed to precisely control the crystal size of MOFs[47−49] in the nanoregime, such as the use of ultrasound and microwave synthesis,[50] microemulsion synthesis,[51] surfactant-mediated hydrothermal syntheses,[52] and coordination modulation methods.[53] Compared to many MOFs, the synthesis of nanocrystals of mesoporous zirconium MOFs is not straightforward. The complexity is due, in part, to the multiple phases that can often be obtained when using the same metal precursor and organic linker in one pot.[54,55] Recently, we developed a method for the synthesis of nanocrystals of mesoporous zirconium MOFs with narrow size distribution and high crystal phase purity.[56] Here, we report the synthesis and characterization of a water-stable *csq-net* zirconium MOF, **NU-1003**, featuring the largest mesoporous aperture known for a zirconium MOF to date. By encapsulating OPAA in crystals of 300 nm length, we have significantly improved the overall initial turnover rate for the hydrolysis of the nerve agent simulant, diisopropyl fluorophosphate (DFP), and the agent itself, Soman (GD). Indeed, the turnover frequencies and overall hydrolysis rates observed for encapsulated OPAA now exceed even those measured for the free enzyme under the same conditions.

RESULTS AND DISCUSSION

Synthesis and Characterization of NU-1003. Recently, we reported the use of a mesoporous zirconium-based MOF,

NU-1000, with *csq-net* topology for enzyme immobilization.[38] Based on the principle of isoreticular design,[57] extending the pore and aperture size in *csq-net* topology zirconium MOFs should be possible by using longer linkers. However, previous attempts to extend the pore and aperture size of **NU-1000** by adding C−C single or triple bonds[58,59] between neighboring phenyl rings resulted in an isomorphic zirconium MOF with *ftw* topology.[60] In order to address this challenge, we designed and synthesized (Figure 1a and Scheme S1) a tetracarboxylate
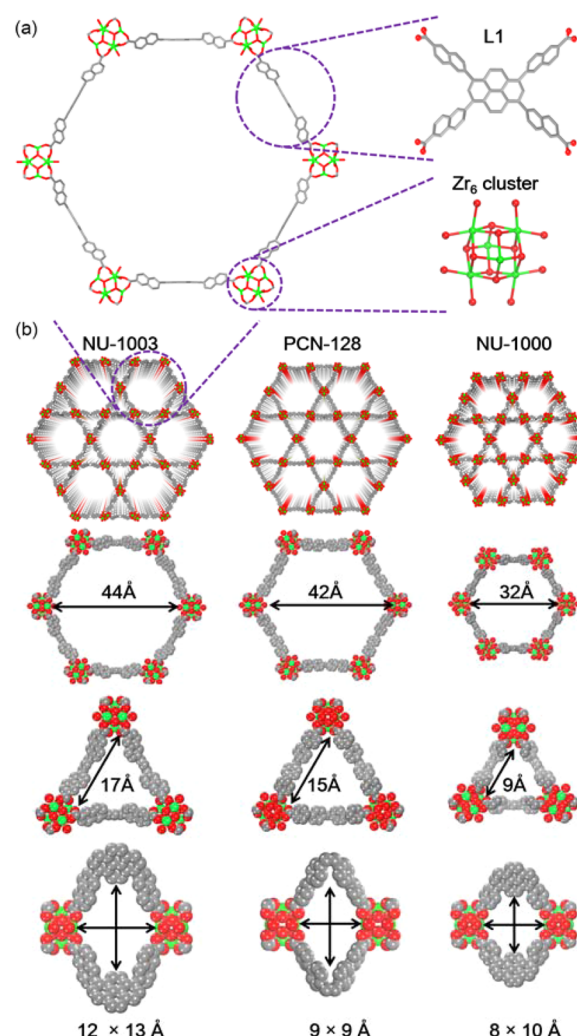

Figure 1. (a) Simulated crystal structure of NU-1003 composed of tetratopic pyrene-based linker L1 and a Zr$_6$ cluster. (b) Packing diagram, hexagonal pores, triangular pores, and windows between hexagonal/triangular pores in NU-1003 (left), PCN-128 (middle), and NU-1000 (right) (Zr atoms are shown in green, C atoms in gray, and O atoms in red; H atoms are omitted for clarity). The pore lengths and diameters are measured between the two closest atoms in the direction of the arrows, taking into account the van der Waals radii of atoms.

linker **L1** based on pyrene. The solvothermal reaction of zirconyl chloride octahydrate with **L1** in dimethylformamide (DMF) in the presence of a trifluoroacetic acid (TFA) modulator indeed afforded rod-like microcrystals (Figure S1) of **NU-1003**. However, the crystals were too small to obtain an experimental single-crystal structure of **NU-1003**.

Previously, we developed a method for obtaining crystal structures from powder X-ray diffraction (PXRD) data by
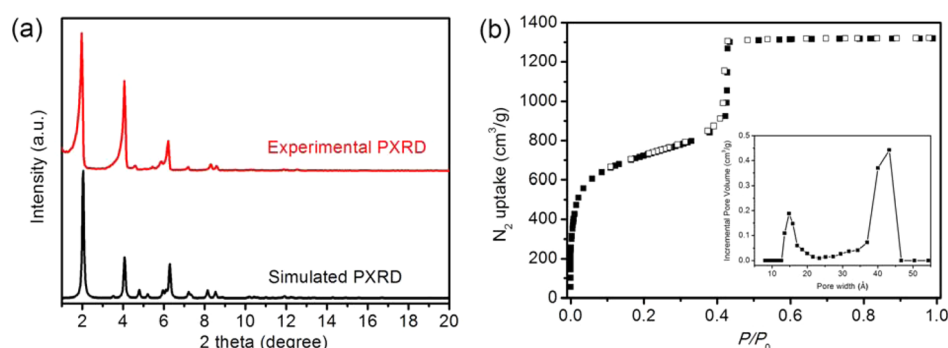
Figure 2. (a) Experimental and simulated PXRD patterns; (b) N_2 isotherm of NU-1003 at 77K (inset: DFT pore size distribution) after activation by SCD.
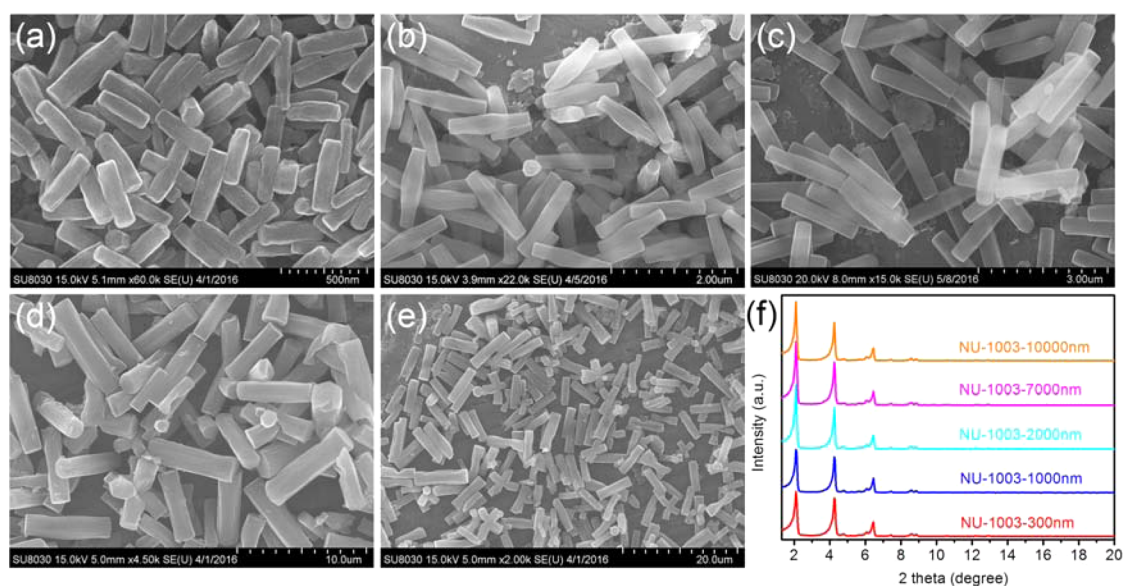

Figure 3. Scanning electron microscopy images of NU-1003 crystals with lengths of (a) 300, (b) 1000, (c) 2000, (d) 7000, and (e) 10000 nm. (f) PXRD patterns of different sizes of NU-1003 crystals.

combining *in silico* construction of MOF structures and simulation of their PXRD patterns along with classical force-field structural optimization. This method has been used to simulate zirconium MOF structures by using the well-defined $Zr_6(\mu_3\text{-}O)_4(\mu_3\text{-}OH)_4(OH)_4(H_2O)_4$ (Zr_6 cluster) node and tetracarboxylate linkers.[58,61] In accordance with the experimental PXRD pattern for the NU-1003, a P1 structure was found computationally (Figure 2a). This simulated structure is composed of 8-connected Zr_6 cluster nodes and L1 linkers (Figure 1a) and features an extended *csq-net* topology. In comparison to Figure 1b, notably, the diameters of the hexagonal pores (44 Å) of NU-1003 are larger than those of previously reported *csq-net* zirconium MOFs, including the mesoporous MOFs PCN-128[42] (42 Å) and NU-1000 (32 Å).[41] The side length of the triangular pores (17 Å) of NU-1003 is also larger than that of PCN-128 (15 Å) and much larger than that of NU-1000 (9 Å). Most importantly, for NU-1003, the size of the windows (12 × 13 Å) between hexagonal and triangular pores is much larger than both PCN-128 (9 × 9 Å) and NU-1000 (8 × 10 Å). These larger micropores and windows between micro- and mesopores (one-dimensional channels) can aid with the diffusive transport of molecular substrate and product after enzyme immobilization selectively in the mesopores of NU-1003. After activation using

supercritical drying (SCD) with CO_2,[14,62] the BET area[63] (Figure S2) obtained from the measured N_2 isotherm (Figure 2b) for NU-1003 is 2700 m^2/g. The calculated density functional theory (DFT) pore size distribution (PSD) from the experimental N_2 isotherm indicates that there exist both mesopores (between 3.8 and 4.5 nm) and micropores (between 1.3 and 1.7 nm) in NU-1003. To the our knowledge, NU-1003 presents the largest pore aperture among all zirconium MOFs reported to date.[54]

Based on the previously reported method for synthesizing nanocrystals of zirconium MOFs with *csq-net* topology,[56,64] we were able to obtain hexagonal cylinder-shaped NU-1003 crystals with lengths ranging from 300 to 10000 nm (Figure 3a−e); denoted here as NU-1003-size (size = 300, 1000, 2000, 7000, and 10000 nm). The bulk-phase PXRD patterns of different sizes of NU-1003 crystals are in excellent agreement with the simulated patterns (Figure 3f).

Immobilization of OPAA. To monitor the immobilization process of OPAA in NU-1003, NU-1003-10000nm crystals were soaked in solution with AlexaFluor-647-tagged OPAA (OPAA647) (Figure 4a). *In situ* confocal laser scanning microscopy (CLSM) images on a single crystal of NU-1003-10000nm were taken at 2, 60, 240, 960, 1440, 2880, 4320, and 7200 min (Figure 4b). Using the line tool in ImageJ,[65]
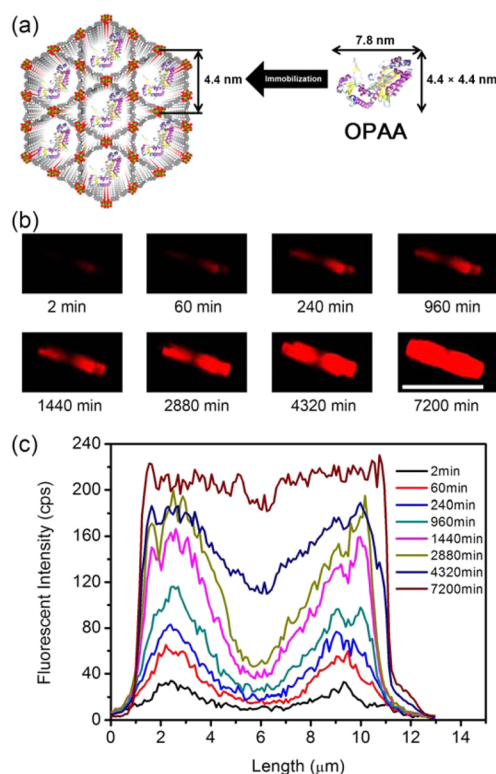
Figure 4. (a) Schematic representation of immobilization of OPAA in the mesoporous channels of NU-1003. (b) CLSM images of a single crystal of OPAA@NU-1003-10000nm with time (scale bar is 10 μm). (c) Plots of fluorescence intensity along a single crystal of OPAA@NU-1003-10000nm with time.

fluorescence intensity profiles taken along the middle of an NU-1003-10000nm crystal with time were obtained and plotted as a function of the length of the crystal (Figure 4c). The results indicate that the diffusion of OPAA647 is one-dimensional from the two ends toward the center of the NU-1003-10000nm crystals. To determine the accurate loading capacity of OPAA in NU-1003, the crystals of NU-1003-size (size = 300, 1000, 2000, 7000, and 10000 nm) were immersed in an aqueous bis-tris-propane buffer (BTP, pH 7.2) solution of OPAA (0.2 mg/mL) at 25 °C. The uptake of OPAA by different sizes of NU-1003 was followed using UV−vis spectroscopy, and the maximum loadings of OPAA for different sizes of NU-1003 varied in the range of 0.12−0.20 mg/mg (Figure 5). These loading capacities were confirmed by inductively coupled plasma optical emission spectroscopy (ICP-OES) measurements of Zr (Zr nodes in the MOF) and S (methionine and cysteine residues in OPAA). The loading profiles of OPAA with different sizes of NU-1003 indicate that the loading rate is generally inversely correlated with the size of the NU-1003 crystals, as one would expect for a primarily diffusive process. To compare the activity of OPAA immobilized in different sizes of NU-1003 crystals, we prepared subsaturated OPAA@NU-1003-size (size = 300, 1000, 2000, 7000, and 10000 nm) using a 0.1 mg/mL initial solution of OPAA (Figure 5b). After completion of immobilization (we allowed 3 days for all), the solid samples were centrifuged and then washed with BTP buffer solution to remove the OPAA adsorbed only on the surface. Not surprisingly, the N$_2$ adsorption isotherms of OPAA@NU-1003-size (size = 300, 1000, 2000, 7000, and 10000 nm) exhibit less N$_2$ uptake than

do enzyme-free samples of NU-1003-size (size = 300, 1000, 2000, 7000, and 10000 nm) (Figure S3). The DFT PSD analyses of NU-1003-size and OPAA@NU-1003-size (size = 300, 1000, 2000, 7000, and 10000 nm) show that the pore volumes corresponding to the triangular channels (1.3−1.6 nm) of NU-1003 drop from 0.20 to 0.15 cm^3/g, while the incremental pore volumes corresponding to the hexagonal channels (3.8−4.6 nm) drop from 0.45 to 0.14 cm^3/g after OPAA immobilization (Figure S4). These results suggest that a large amount of space in the mesopores in NU-1003 is filled by OPAA, while the micropores are relatively unoccupied. The PXRD patterns (Figure S5) and scanning electron microscopy (SEM) images (Figure S6) of different sizes of NU-1003 after OPAA immobilization confirm that bulk crystallinity and morphology are retained. To determine the distribution of OPAA in NU-1003-size crystals, we used SEM with energy-dispersive X-ray (EDX) spectroscopy to assess the distribution of sulfur along single crystals of NU-1003-size (size = 300, 1000, 2000, 7000, and 10000 nm); these measurements confirm, for the full range of crystallites sizes, that OPAA is evenly dispersed (Figure 5c−f).

Size Effect on Nerve Agent Hydrolysis. We next examined the enzyme activity after immobilization and the effect of particle size on DFP hydrolysis (Figure 6a). Although the Zr$_6$ cluster of NU-1003 is identical to those well-studied for nerve agent hydrolysis,[56,66] at pH 7.2 or lower, NU-1003 does not show catalytic activity for the degradation of DFP. Compared to free OPAA under the same conditions, OPAA@NU-1003-7000nm shows a much slower initial hydrolysis rate based on the first data point taken at 2 min.[11] Nevertheless, by using smaller particles, NU-1003-2000nm and NU-1003-1000nm, the hydrolysis rate was significantly increased and became close to that of free OPAA with the conversion of DFP plateauing at 90%. Importantly, when NU-1003-300nm was used as the enzyme carrier, the conversion of DFP reached 100% after only 2 min under the same conditions. Encouraged by the fast hydrolysis rate for DFP using OPAA@NU-1003-300 nm, we tested the performance of OPAA@NU-1003-300 nm on a G-type nerve agent Soman (GD). In BTP pH 7.2 buffer, the degradation of GD catalyzed by OPAA@NU-1003-300nm was complete after 30 min with an initial half-life of $t_{1/2}$ = 2 min (Figure 6b). To accurately compare the initial turnover rate of free OPAA and OPAA@NU-1003-300nm, the half-life of GD was determined by monitoring the release of free fluoride into the BTP buffer (pH 7.2), using a fluoride electrode (Figure 6c). As a control, OPAA@NU-1003-7000nm was also examined. Similar to the findings for DFP hydrolysis, the hydrolysis rate of OPAA@NU-1003-7000 nm (189 μmol/min/mg) is much slower than that of free OPAA (305 μmol/min/mg). Remarkably, the results also indicate that OPAA@NU-1003-300nm can efficiently defluorinate/deactivate Soman with an initial reaction rate of 961 μmol/min/mg (Figure 6d), which is more than 3 times faster than that of free OPAA.

The significantly increased overall turnover rate accompanying the reduction in size of the MOF-based enzyme carrier indicates that the inherent barriers to diffusive permeation of the carrier by molecular reactants and products can be substantially negated by decreasing *in-crystal* diffusion lengths and thereby rendering a larger fraction of the encapsulated enzyme accessible for catalytic hydrolysis. The finding that OPAA@NU-1003-300nm catalyzes the hydrolysis of GD at a rate more than 3 times that of free enzyme may point to a
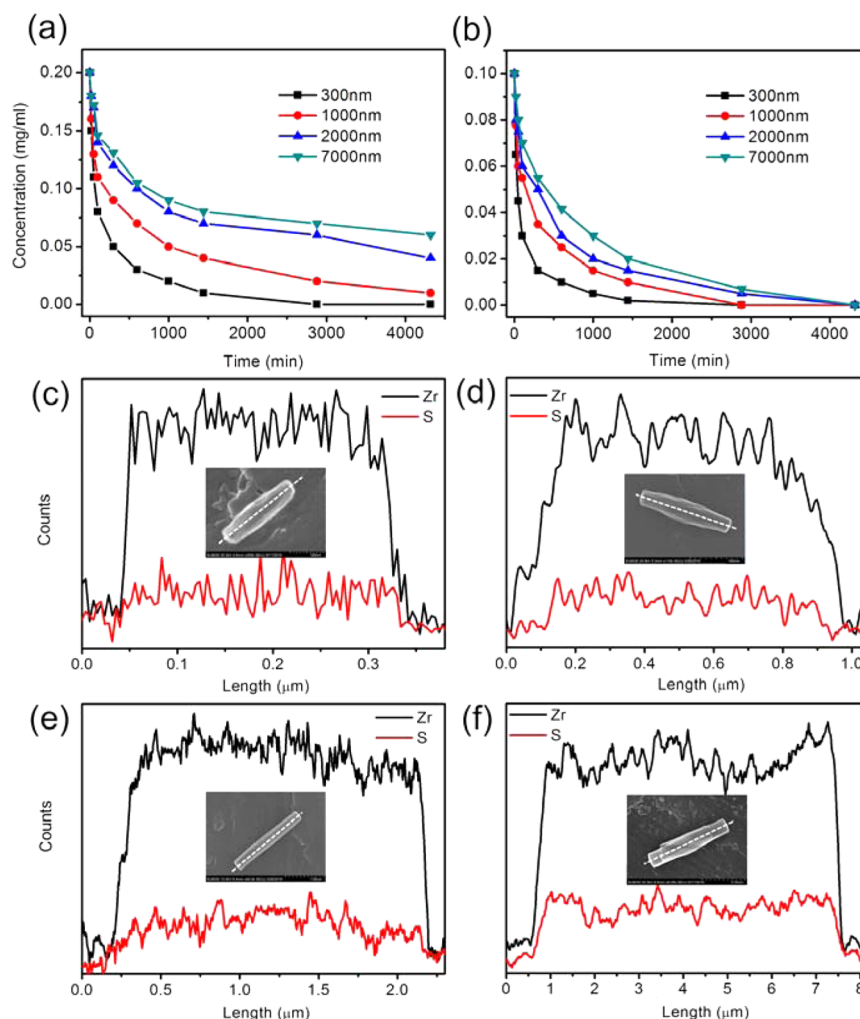
Figure 5. OPAA concentration in the supernatant after soaking different sizes of NU-1003 in the buffer solution of (a) 0.2 mg/mL OPAA and (b) 0.1 mg/mL OPAA; SEM images and EDX spectra of a single crystal of (c) OPAA@NU-1003-300nm, (d) OPAA@NU-1003-1000nm, (e) OPAA@NU-1003-2000nm, and (f) OPAA@NU-1003-7000nm. EDX line scans for Zr and S are in black and red, respectively. The dashed white lines indicate where the EDX scan was taken.

beneficial confinement effect upon the enzyme's intrinsic activity. Alternatively, the enhancement may be indicative of elimination of previously unrecognized residual aggregation (and deactivation) in the solution phase. Regardless, such a large increase is significant as the OPAA enzyme already exhibits the highest reported GD activity of any enzyme known to us.

Finally, it should be noted that BTP buffer was intentionally chosen for the catalysis studies because its pH of 7.2 is close to that of human blood.[67] The obtained results suggest that nanosized **OPAA@NU-1003** has potential for use as an injectable antidotal formulation in the human body for highly efficient nerve agent hydrolysis. To realize that goal, surface modification of the nanosized **OPAA@NU-1003** with biocompatible molecules will likely be necessary and, as such, is currently under investigation.

CONCLUSIONS

In summary, we have designed and prepared a water-stable zirconium metal−organic framework, **NU-1003**. This MOF features a *csq-net* topology and has the largest mesoporous apertures (4.6 nm) known for a zirconium MOF to date. In addition, the size of **NU-1003** crystals is tunable from 300 to

10000 nm. We have also studied and shown that a nerve agent hydrolyzing enzyme, OPAA, can be encapsulated in the pores of **NU-1003** and the catalytic efficiency of the immobilized OPAA in the nanosized MOF is significantly increased compared to that of free OPAA in BTP buffer. This report highlights a method for the highly efficient hydrolysis of a nerve agent using a nanosized enzyme carrier and the nanosized MOF−enzyme carriers could be used as a formulation for *in vivo* nerve agent degradation in the future.

METHODS

Materials. ZrOCl$_2$·8H$_2$O (98%), benzoic acid (>99.5%), 1,3,6,8-tetrabromopyrene (97%), diisopropyl fluorophosphate, bis-tris-propane, potassium hydroxide (90%), potassium phosphate tribasic (>98%), dioxane (>99.0%), and trifluoroacetic acid (99%) were purchased from Sigma-Aldrich. Tetrakis(triphenylphosphine)-palladium(0) (99%) was purchased from Strem Chemicals. *N,N'*-Dimethylformamide (99.8%) was obtained from Macron Fine Chemicals. AlexaFluor-647 dye was purchased from Life Technologies (Thermo Fisher Scientific). Methyl 6-(pinacolboryl)-2-naphthoate was synthesized using a published procedure.[68] All chemicals were used without further purification. The gene encoding the OPAA enzyme was originally cloned from *Alteromonas* sp. JD6.5, as described previously.[7] GD was from our stocks at the Edgewood Chemical
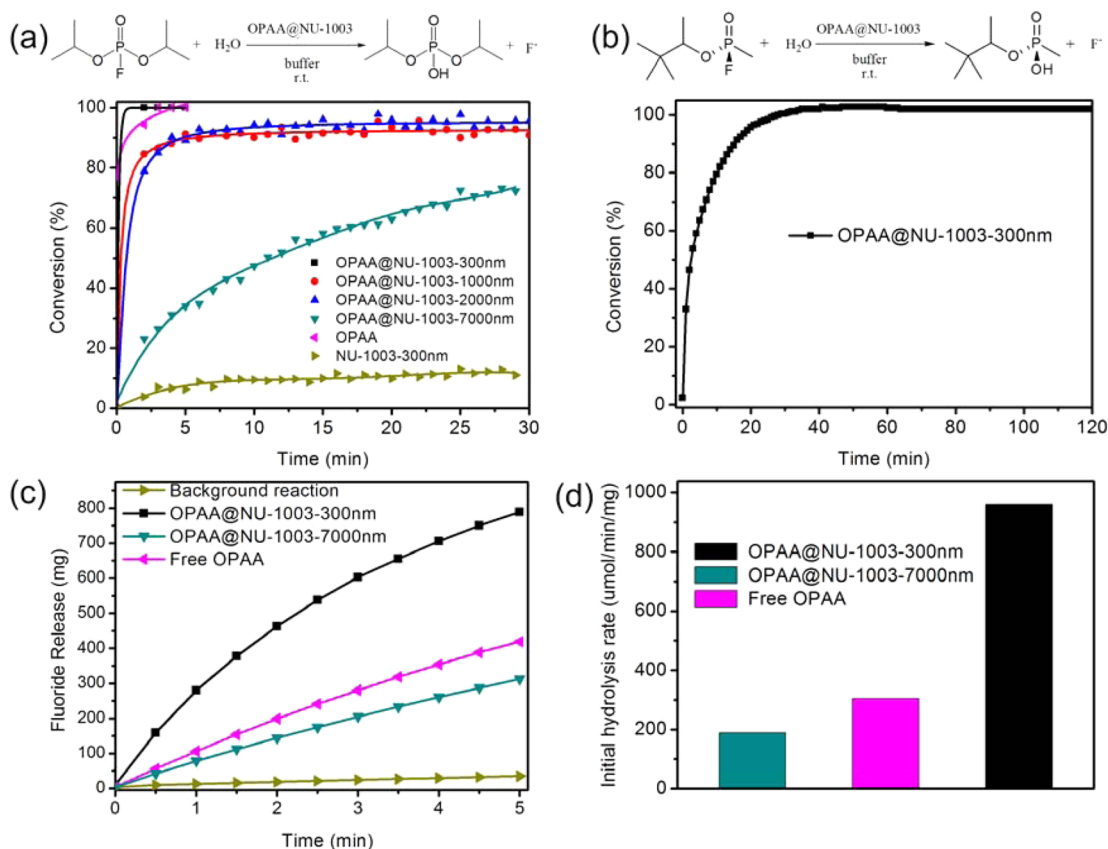
Figure 6. (a) Hydrolysis profiles of DFP catalyzed by different sizes of OPAA@NU-1003. (b) Full hydrolysis curve of GD catalyzed by OPAA@NU-1003-300nm. (c) Hydrolysis profiles of GD catalyzed by OPAA@NU-1003-300nm, OPAA@NU-1003-7000nm, free OPAA, and the background reaction in the first 5 min. (d) Initial turnover rate of OPAA@NU-1003-300nm, OPAA@NU-1003-7000nm, and free OPAA for hydrolysis of GD.

Biological Center and was 95.3 ± 1.5% pure by ^{31}P NMR, NIST-traceable through an internal triethylphosphate standard.

Physical Methods and Measurements. Powder X-ray diffraction spectra were collected on a Rigaku model Smartlab diffractometer equipped with a Cu rotating anode X-ray source. N_2 sorption isotherm measurements were performed on a Micromeritics Tristar II 3020 (Micromeritics, Norcross, GA) at 77 K. ^{31}P NMR specta were recorded on an Agilent 400 FT-NMR spectrometer (400 MHz). SEM images and EDX profiles were collected on a Hitachi SU8030. Samples were activated and coated with OsO_4 to ∼8 nm thickness in a Denton Desk III TSC sputter coater (Moorestown, NJ) before SEM-EDX analysis. ICP-OES was performed on a computer-controlled (QTEGRA software v. 2.2) Thermo iCap 7600 Duo ICP-OES (Thermo Fisher Scientific, Waltham, MA) operating in standard mode and equipped with a SPRINT valve and CETAC 520 autosampler (Teladyne CETAC, Omaha, NE, USA). **OPAA@NU-1003** samples (2−3 mg) were digested in a small amount (1 mL) of a mixture of 3:1 v/v concentrated HNO_3/H_2O_2 (30 wt % in H_2O) by being heated in a Biotage (Uppsala, Sweden) SPX microwave reactor (software version 2.3, build 6250) at 150 °C for 5 min. The acidic solution was then diluted to a final volume of 15 mL with ultrapure deionized H_2O and analyzed for S (180.731, 182.034, and 182.624 nm) and Zr (339.198, 343.823, and 349.619 nm) content as compared to the standard solutions. The enzymes loading is determined by comparing the experimental Zr/S ratio to the theoretical ratio given by the stoichiometry of Zr in the MOF to the number of methionine and cysteine thiols present in OPAA. Confocal laser scanning microscopy images were taken on a Leica TCS SP5. Electrospray ionization mass spectrometry data were recorded on a Bruker AmaZon SL ion trap at IMSERC (Integrated Molecular Structure Education and Research Center) of Northwestern University.

Synthesis of 1,3,6,8-Tetra(6-methoxycarbonylnaphthalen-2-yl)pyrene (L1-OMe). Dioxane (250 mL) was placed in a 500 mL three-necked round-bottom flask and purged with argon for 1.5 h. With argon purging and the use of a mechanical stirrer, tetrabromopyrene (5.0 g, 9.7 mmol), methyl 6-(pinacolboryl)-2-naphthoate (13.3 g, 42.5 mmol), potassium phosphate tribasic (16.5 g, 77.7 mmol), and tetrakis(triphenylphosphine)palladium(0) (0.55 g, 0.48 mmol) were added. The reaction was heated to 90 °C for 72 h. The reaction mixture was allowed to cool to room temperature, and then 250 mL of water was added. The yellow solid was filtered using a glass Büchner funnel (medium frit) and washed with water (2 × 500 mL), followed by 500 mL of acetone. The filter flask was then emptied, and the solid was collected by passing hot chloroform (6 × 500 mL) through the frit and collecting the filtrate. Purification by flash column chromatography (silica gel) afforded the product as a light yellow solid (5.28 g, 58%). The product was analyzed by ^{1}H NMR spectroscopy: ^{1}H NMR (500 MHz, $CDCl_3$) δ/ppm = 8.71 (s, 4H), 8.25 (s, 4H), 8.21 (s, 2H), 8.19 (s, 4H), 8.14−8.12 (m, 4H), 8.11 (dd, J = 5.8, 3.0 Hz, 4H), 7.98−7.94 (m, 4H), 7.92−7.88 (m, 4H), 4.15−3.87 (m, 12H).

Synthesis of 1,3,6,8-Tetra(6-carboxynaphthalen-2-yl)pyrene (L1). L1-OMe (5g, 5.3 mmol) was added to a 1000 mL single-necked flask, and dioxane (250 mL) was then added while stirring. A solution of potassium hydroxide (3.0 g, 53 mmol; 250 mL of water) was added, and the reaction mixture was heated to reflux while being rigorously stirred for 18 h (at this point, a clear solution was observed). The reaction was allowed to cool to room temperature. The organic solvent was removed using rotary evaporation, and 500 mL of water was added to dissolve the solid obtained. Concentrated HCl was added to the solution dropwise with stirring until the solution reached pH 1. After being stirred for an additional hour, the yellow precipitate was collected *via* centrifugation and washed with water (3 × 50 mL). The

final solid product was recrystallized from DMF, filtered, and dried (3.6 g, 68%). The product was analyzed by ^{1}H NMR and ^{13}C NMR spectroscopy: ^{1}H NMR (500 MHz, DMSO-d_6) δ/ppm = 13.16 (s, 4H), 8.75 (s, 4H), 8.41 (s, 4H), 8.35 (d, J = 8.5 Hz, 4H), 8.31 (m, 6H), 8.15 (d, J = 8.7 Hz, 4H), 8.07 (d, J = 8.5 Hz, 4H), 8.01 (d, J = 8.4 Hz, 4H); ^{13}C NMR (500 MHz, DMSO-d_6) δ 167.92 (s), 140.27 (s), 137.23 (s), 135.51 (s), 131.91 (s), 130.84 (s), 130.67 (s), 129.98 (d), 129.69 (s), 129.18 (s), 129.01 (s), 128.29 (s), 126.31 (s), 126.08 (s), 125.85 (s); MS (ESI+) m/z 881.22 [M − H]$^+$, 882.22 [M], 883.22 [M + H]$^+$.

Synthesis of Different Sizes of NU-1003. A stock solution A was prepared as follows: ZrOCl$_2$·8H$_2$O (200 mg, 0.62 mmol), benzoic acid (2.5 g, 20.5 mmol), and 50 mL of DMF were added into a 250 mL bottle. The solution was heated at 80 °C for 1 h and then allowed to cool to room temperature. **L1** (80 mg, 0.09 mmol) and 50 mL of DMF were added to the 250 mL bottle to form a clear solution.

NU-1003-300nm: To a 20 mL portion of stock solution A in an 8-dram vial, 100 μL of TFA (2.94 mmol) was added and the solution was sonicated for 10 min. The reaction mixture was placed in an oven at 120 °C for 3 h during which time a light yellow suspension was formed.

NU-1003-1000nm: To a 20 mL portion of stock solution A in an 8-dram vial, 200 μL of TFA (5.89 mmol) was added and the solution was sonicated for 10 min. The reaction mixture was then placed in an oven at 120 °C for 3 h during which time a light yellow suspension was formed.

NU-1003-2000nm: To a 20 mL portion of stock solution A in an 8-dram vial, 250 μL of TFA (7.40 mmol) was added and the solution was sonicated for 10 min. The reaction mixture was then placed in an oven at 120 °C for 3 h during which time a light yellow suspension was formed.

NU-1003-7000nm: To a 20 mL portion of stock solution A in an 8-dram vial, 350 μL of TFA (10.30 mmol) was added and the solution was sonicated for 10 min. The reaction mixture was then placed in an oven at 120 °C for 3 h during which time a light yellow suspension was formed.

NU-1003-10000nm: To a 20 mL portion of stock solution A in an 8-dram vial, 500 μL of TFA (14.72 mmol) was added and the solution was sonicated for 10 min. The reaction mixture was then placed in an oven at 120 °C for 3 h during which time a light yellow suspension was formed.

MOF Isolation. In each case (above), the light yellow suspension was centrifuged for 5 min at 7800 rpm. The solid was then washed with fresh DMF (3 × 30 mL) before being soaked in 40 mL of fresh DMF with 40 μL of TFA for 16 h at room temperature. The sample was subsequently washed with fresh DMF (3 × 30 mL) and ethanol (3 × 30 mL).

SCD Activation Procedure.[62] NU-1003 (50 mg) was soaked in absolute ethanol (10 mL), and the soaking solution was replaced six times/day for 3 days. The sample was placed inside a supercritical CO$_2$ dryer, and the ethanol was exchanged with liquid CO$_2$ over a period of 8 h. The liquid CO$_2$ was purged under positive pressure for 3 min every 2 h. The rate of venting of liquid CO$_2$ was always kept below the rate of filling to maintain a full drying chamber. After four purge cycles, the temperature was increased to 38 °C (*i.e.*, above the critical temperature for carbon dioxide), and the chamber was slowly vented over the course of 15 h at a rate of 0.5 mL/min. The activated MOF was then stored inside an inert atmosphere glovebox until further analysis.

Porosity Measurements. The SCD-activated MOF material (50−100 mg) was evacuated on a SmartVacPrep instrument (Micromeritics Instrument Corporation, Norcross, GA) under dynamic vacuum (10^{-5} Torr) at room temperature for 7 h followed by 30 °C for 1 h, 50 °C for 1 h, 70 °C for 1 h, and then 80 °C for 15 h. Nitrogen adsorption isotherm measurements were carried out on a Micromeritics Tristar II 3020 (Micromeritics Instrument Corporation) at 77 K. Pore size distributions were obtained by DFT calculations using a carbon slit-pore model with a N$_2$ kernel. Particle size and phase purity of **NU-1003** were characterized using SEM (SU8030, Hitachi) and PXRD (Smartlab, Rigaku).

Labeling OPAA with Fluorescent Dye. AlexaFluor-647-labeled OPAA (OPAA647) was prepared by reacting OPAA (0.5 mg, 10 nmol) with 1.2 equiv of an AlexaFluor-647−(ethyl-*p*-nitrophenyl)-phosphonate conjugate followed by purification of the labeled protein by size-exclusion chromatography.

OPAA Immobilization in NU-1003. NU-1003-size (1 mg) (size = 300, 1000, 2000, and 7000 nm) was added to 1 mL of deionized water and sonicated for 5 min until a uniform suspension was formed. The well-dispersed solid was isolated by centrifugation at 15000 rpm for 1 min, and the supernatant was decanted. The solid was then suspended in a 1 mL solution of OPAA (0.2 mg/mL for saturated samples or 0.1 mg/mL for subsaturated samples) in BTP buffer solution (pH 7.2). The absorbance of the supernatant solution at 280 nm was recorded over 72 h using a NanoDrop 2000 UV−vis spectrophotometer. The **OPAA@NU-1003-size** (size = 300, 1000, 2000, and 7000 nm) composites were isolated by centrifugation at 15000 rpm for 1 min, and the supernatant was removed. The solid was further washed with BTP buffer (pH 7.2) (5 × 1 mL) before further experiments.

Catalytic Reaction Experiments. *Hydrolysis Activity for DFP:* Hydrolysis profiles of DFP using free OPAA or immobilized **OPAA@ NU-1003** were recorded on an Agilent 400 FT-NMR spectrometer (400 MHz) based on the ^{31}P NMR spectrum. The ^{31}P NMR spectrum for DFP consists of a doublet (−7.62 and −13.69 ppm) due to the phosphorus−fluorine coupling. After the phosphorus−fluorine bond is hydrolyzed by OPAA, the spectrum consists entirely of a downfield singlet from the diisopropylphosphate (−0.95 ppm). For a typical reaction, the **OPAA@NU-1003** composite (0.1 mg of OPAA and 1 mg of **NU-1003**) was loaded into a 1.5-dram vial. Then 896 μL of BTP buffer (pH 7.2) and 100 μL of deuterated water were added, and the reaction mixture was stirred for 1 min to disperse the MOF crystals homogeneously. Four microliters (22 μmol) of DFP was then added, and the reaction mixture was swirled for 10 s. The reaction mixture was then transferred to an NMR tube, and the ^{31}P NMR spectrum was immediately measured; the first data point was collected 120 s after the start of the reaction. The progress of the reaction was monitored with 1 min increments for 30 min (number of scans = 16, delay time = 28 s). The degree of completion was assessed by calculating the ratio between integration of the product and the reactant peaks in the ^{31}P NMR spectra (percent conversion = product peak integral/(substrate + product peak integral) × 100).

Hydrolysis Activity for GD: The reaction rates for Soman (GD) were determined by monitoring the release of free fluoride at 25 °C in 50 mM bis-tris-propane buffer, pH 7.2, using a fluoride electrode with fixed initial 3.0 mM GD concentration.

ASSOCIATED CONTENT

Ⓢ Supporting Information

The Supporting Information is available free of charge on the ACS Publications website at DOI: 10.1021/acsnano.6b04996.

> Supplementary SEM images, N$_2$ isotherms, PXRD patterns, NMR spectra, and mass spectra (PDF)
> Computational construction of **NU-1003** (CIF)

AUTHOR INFORMATION

Corresponding Author

*E-mail: o-farha@northwestern.edu.

Notes

The authors declare no competing financial interest.

ACKNOWLEDGMENTS

REFERENCES

(1) Raushel, F. M. Chemical Biology: Catalytic Detoxification. *Nature* **2011**, *469* (7330), 310−311.

(2) Tsai, P.-C.; Fox, N.; Bigley, A. N.; Harvey, S. P.; Barondeau, D. P.; Raushel, F. M. Enzymes for the Homeland Defense: Optimizing Phosphotriesterase for the Hydrolysis of Organophosphate Nerve Agents. *Biochemistry* **2012**, *51* (32), 6463−6475.

(3) Newmark, J. Therapy for Nerve Agent Poisoning. *Arch. Neurol.* **2004**, *61* (5), 649−652.

(4) Nachon, F.; Brazzolotto, X.; Trovaslet, M.; Masson, P. Progress in the Development of Enzyme-Based Nerve Agent Bioscavengers. *Chem.-Biol. Interact.* **2013**, *206* (3), 536−544.

(5) Firozjaei, S. A. A.; Latifi, A. M.; Khodi, S.; Abolmaali, S.; Choopani, A. A Review on Biodegradation of Toxic Organophosphate Compounds. *J. Appl. Biotechnol. Rep.* **2015**, *2* (2), 215−224.

(6) Ghanem, E.; Raushel, F. M. Detoxification of Organophosphate Nerve Agents by Bacterial Phosphotriesterase. *Toxicol. Appl. Pharmacol.* **2005**, *207* (2), 459−470.

(7) Daczkowski, C. M.; Pegan, S. D.; Harvey, S. P. Engineering the Organophosphorus Acid Anhydrolase Enzyme for Increased Catalytic Efficiency and Broadened Stereospecificity on Russian Vx. *Biochemistry* **2015**, *54* (41), 6423−6433.

(8) Petrikovics, I.; Papahadjopoulos, D.; Hong, K.; Cheng, T. C.; Baskin, S. I.; Jiang, J.; Jaszberenyi, J. C.; Logue, B. A.; Szilasi, M.; McGuinn, W. D. Comparing Therapeutic and Prophylactic Protection against the Lethal Effect of Paraoxon. *Toxicol. Sci.* **2004**, *77* (2), 258−262.

(9) Kernchen, R. J. Enzyme Stabilization in Nanostructured Materials, for Use in Organophosphorus Nerve Agent Detoxification and Prophylaxis. In *Biodefence*; Springer: Berlin, 2011; pp 135−145.

(10) Petrikovics, I.; Cheng, T.-C.; Papahadjopoulos, D.; Hong, K.; Yin, R.; DeFrank, J.; Jaing, J.; Song, Z.; McGuinn, W.; Sylvester, D. Long Circulating Liposomes Encapsulating Organophosphorus Acid Anhydrolase in Diisopropylfluorophosphate Antagonism. *Toxicol. Sci.* **2000**, *57* (1), 16−21.

(11) Li, P.; Moon, S.-Y.; Guelta, M. A.; Harvey, S. P.; Hupp, J. T.; Farha, O. K. Encapsulation of a Nerve Agent Detoxifying Enzyme by a Mesoporous Zirconium Metal-Organic Framework Engenders Thermal and Long-Term Stability. *J. Am. Chem. Soc.* **2016**, *138* (26), 8052−8055.

(12) Furukawa, H.; Cordova, K. E.; O'Keeffe, M.; Yaghi, O. M. The Chemistry and Applications of Metal-Organic Frameworks. *Science* **2013**, *341* (6149), 1230444.

(13) Murray, L. J.; Dincă, M.; Long, J. R. Hydrogen Storage in Metal−Organic Frameworks. *Chem. Soc. Rev.* **2009**, *38* (5), 1294−1314.

(14) Farha, O. K.; Yazaydın, A. Ö.; Eryazici, I.; Malliakas, C. D.; Hauser, B. G.; Kanatzidis, M. G.; Nguyen, S. T.; Snurr, R. Q.; Hupp, J. T. De Novo Synthesis of a Metal−Organic Framework Material Featuring Ultrahigh Surface Area and Gas Storage Capacities. *Nat. Chem.* **2010**, *2* (11), 944−948.

(15) Kreno, L. E.; Leong, K.; Farha, O. K.; Allendorf, M.; Van Duyne, R. P.; Hupp, J. T. Metal−Organic Framework Materials as Chemical Sensors. *Chem. Rev.* **2012**, *112* (2), 1105−1125.

(16) Hu, Z.; Deibert, B. J.; Li, J. Luminescent Metal−Organic Frameworks for Chemical Sensing and Explosive Detection. *Chem. Soc. Rev.* **2014**, *43* (16), 5815−5840.

(17) Chen, B.; Xiang, S.; Qian, G. Metal− Organic Frameworks with Functional Pores for Recognition of Small Molecules. *Acc. Chem. Res.* **2010**, *43* (8), 1115−1124.

(18) Li, J.-R.; Sculley, J.; Zhou, H.-C. Metal−Organic Frameworks for Separations. *Chem. Rev.* **2012**, *112* (2), 869−932.

(19) Li, J.-R.; Kuppler, R. J.; Zhou, H.-C. Selective Gas Adsorption and Separation in Metal−Organic Frameworks. *Chem. Soc. Rev.* **2009**, *38* (5), 1477−1504.

(20) Chen, B.; Wang, L.; Xiao, Y.; Fronczek, F. R.; Xue, M.; Cui, Y.; Qian, G. A Luminescent Metal−Organic Framework with Lewis Basic Pyridyl Sites for the Sensing of Metal Ions. *Angew. Chem., Int. Ed.* **2009**, *48* (3), 500−503.

(21) Howarth, A. J.; Katz, M. J.; Wang, T. C.; Platero-Prats, A. E.; Chapman, K. W.; Hupp, J. T.; Farha, O. K. High Efficiency Adsorption and Removal of Selenate and Selenite from Water Using Metal-Organic Frameworks. *J. Am. Chem. Soc.* **2015**, *137* (23), 7488−7494.

(22) Furukawa, H.; Ko, N.; Go, Y. B.; Aratani, N.; Choi, S. B.; Choi, E.; Yazaydin, A. Ö.; Snurr, R. Q.; O'Keeffe, M.; Kim, J.; et al. Ultrahigh Porosity in Metal-Organic Frameworks. *Science* **2010**, *329* (5990), 424−428.

(23) Bloch, E. D.; Queen, W. L.; Krishna, R.; Zadrozny, J. M.; Brown, C. M.; Long, J. R. Hydrocarbon Separations in a Metal-Organic Framework with Open Iron (Ii) Coordination Sites. *Science* **2012**, *335* (6076), 1606−1610.

(24) Liu, Y.; Xuan, W.; Cui, Y. Engineering Homochiral Metal-Organic Frameworks for Heterogeneous Asymmetric Catalysis and Enantioselective Separation. *Adv. Mater.* **2010**, *22* (37), 4112−4135.

(25) Yabushita, M.; Li, P.; Bernales, V.; Kobayashi, H.; Fukuoka, A.; Gagliardi, L.; Farha, O. K.; Katz, A. Unprecedented Selectivity in Molecular Recognition of Carbohydrates by a Metal-Organic Framework. *Chem. Commun.* **2016**, *52*, 7094−7097.

(26) Wang, X.; Lu, W.; Gu, Z.-Y.; Wei, Z.; Zhou, H.-C. Topology-Guided Design of an Anionic Bor-Network for Photocatalytic [Ru (Bpy) 3] 2+ Encapsulation. *Chem. Commun.* **2016**, *52* (9), 1926−1929.

(27) Li, B.; Zhang, Y.; Ma, D.; Ma, T.; Shi, Z.; Ma, S. Metal-Cation-Directed De Novo Assembly of a Functionalized Guest Molecule in the Nanospace of a Metal-Organic Framework. *J. Am. Chem. Soc.* **2014**, *136* (4), 1202−1205.

(28) Howarth, A. J.; Liu, Y.; Li, P.; Li, Z.; Wang, T. C.; Hupp, J. T.; Farha, O. K. Chemical, Thermal and Mechanical Stabilities of Metal-Organic Frameworks. *Nat. Rev. Mater.* **2016**, *1*, 15018.

(29) Shieh, F. K.; Wang, S. C.; Yen, C. I.; Wu, C. C.; Dutta, S.; Chou, L. Y.; Morabito, J. V.; Hu, P.; Hsu, M. H.; Wu, K. C. W.; Tsung, C. K. Imparting Functionality to Biocatalysts Via Embedding Enzymes into Nanoporous Materials by a De Novo Approach: Size-Selective Sheltering of Catalase in Metal-Organic Framework Microcrystals. *J. Am. Chem. Soc.* **2015**, *137* (13), 4276−4279.

(30) Liang, K.; Ricco, R.; Doherty, C. M.; Styles, M. J.; Bell, S.; Kirby, N.; Mudie, S.; Haylock, D.; Hill, A. J.; Doonan, C. J.; et al. Biomimetic Mineralization of Metal-Organic Frameworks as Protective Coatings for Biomacromolecules. *Nat. Commun.* **2015**, *6*, 7240.

(31) Deng, H.; Grunder, S.; Cordova, K. E.; Valente, C.; Furukawa, H.; Hmadeh, M.; Gándara, F.; Whalley, A. C.; Liu, Z.; Asahina, S.; Kazumori, H.; O'Keeffe, M.; Terasaki, O.; Stoddart, J. F.; Yaghi, O. M. Large-Pore Apertures in a Series of Metal-Organic Frameworks. *Science* **2012**, *336* (6084), 1018−1023.

(32) Chen, Y.; Lykourinou, V.; Hoang, T.; Ming, L.-J.; Ma, S. Size-Selective Biocatalysis of Myoglobin Immobilized into a Mesoporous Metal−Organic Framework with Hierarchical Pore Sizes. *Inorg. Chem.* **2012**, *51* (17), 9156−9158.

(33) Lykourinou, V.; Chen, Y.; Wang, X.-S.; Meng, L.; Hoang, T.; Ming, L.-J.; Musselman, R. L.; Ma, S. Immobilization of Mp-11 into a Mesoporous Metal-Organic Framework, Mp-11@ Mesomof: A New Platform for Enzymatic Catalysis. *J. Am. Chem. Soc.* **2011**, *133* (27), 10382−10385.

(34) Lyu, F.; Zhang, Y.; Zare, R. N.; Ge, J.; Liu, Z. One-Pot Synthesis of Protein-Embedded Metal-Organic Frameworks with Enhanced Biological Activities. *Nano Lett.* **2014**, *14* (10), 5761−5765.

(35) Feng, D.; Liu, T.-F.; Su, J.; Bosch, M.; Wei, Z.; Wan, W.; Yuan, D.; Chen, Y.-P.; Wang, X.; Wang, K.; Lian, X.; Gu, Z.-Y.; Park, J.; Zou, X.; Zhou, H.-C. Stable Metal-Organic Frameworks Containing Single-Molecule Traps for Enzyme Encapsulation. *Nat. Commun.* **2015**, *6*, 5979.

(36) Mehta, J.; Bhardwaj, N.; Bhardwaj, S. K.; Kim, K.-H.; Deep, A. Recent Advances in Enzyme Immobilization Techniques: Metal-Organic Frameworks as Novel Substrates. *Coord. Chem. Rev.* **2016**, *322*, 30–40.

(37) Wu, X.; Hou, M.; Ge, J. Metal−Organic Frameworks and Inorganic Nanoflowers: A Type of Emerging Inorganic Crystal Nanocarrier for Enzyme Immobilization. *Catal. Sci. Technol.* **2015**, *5* (12), 5077–5085.

(38) Li, P.; Modica, J. A.; Howarth, A. J.; Vargas, E.; Moghadam, P. Z.; Snurr, R. Q.; Mrksich, M.; Hupp, J. T.; Farha, O. K. Toward Design Rules for Enzyme Immobilization in Hierarchical Mesoporous Metal-Organic Frameworks. *Chem.* **2016**, *1* (1), 154–169.

(39) Morris, W.; Volosskiy, B.; Demir, S.; Gándara, F.; McGrier, P. L.; Furukawa, H.; Cascio, D.; Stoddart, J. F.; Yaghi, O. M. Synthesis, Structure, and Metalation of Two New Highly Porous Zirconium Metal−Organic Frameworks. *Inorg. Chem.* **2012**, *51* (12), 6443–6445.

(40) Feng, D.; Gu, Z.-Y.; Li, J.-R.; Jiang, H.-L.; Wei, Z.; Zhou, H.-C. Zirconium-Metalloporphyrin Pcn-222: Mesoporous Metal−Organic Frameworks with Ultrahigh Stability as Biomimetic Catalysts. *Angew. Chem., Int. Ed.* **2012**, *51* (41), 10307–10310.

(41) Mondloch, J. E.; Bury, W.; Fairen-Jimenez, D.; Kwon, S.; DeMarco, E. J.; Weston, M. H.; Sarjeant, A. A.; Nguyen, S. T.; Stair, P. C.; Snurr, R. Q.; et al. Vapor-Phase Metalation by Atomic Layer Deposition in a Metal−Organic Framework. *J. Am. Chem. Soc.* **2013**, *135* (28), 10294–10297.

(42) Zhang, Q.; Su, J.; Feng, D.; Wei, Z.; Zou, X.; Zhou, H.-C. Piezofluorochromic Metal−Organic Framework: A Microscissor Lift. *J. Am. Chem. Soc.* **2015**, *137* (32), 10064–10067.

(43) Wang, K.; Feng, D.; Liu, T.-F.; Su, J.; Yuan, S.; Chen, Y.-P.; Bosch, M.; Zou, X.; Zhou, H.-C. A Series of Highly Stable Mesoporous Metalloporphyrin Fe-Mofs. *J. Am. Chem. Soc.* **2014**, *136* (40), 13983–13986.

(44) Lo, S.-H.; Chien, C.-H.; Lai, Y.-L.; Yang, C.-C.; Lee, J. J.; Raja, D. S.; Lin, C.-H. A Mesoporous Aluminium Metal-Organic Framework with 3 Nm Open Pores. *J. Mater. Chem. A* **2013**, *1* (2), 324–329.

(45) Hanefeld, U.; Gardossi, L.; Magner, E. Understanding Enzyme Immobilisation. *Chem. Soc. Rev.* **2009**, *38* (2), 453–468.

(46) Fogler, H. S. *Elements of Chemical Reaction Engineering*; Prentice-Hall International: London, 1999.

(47) Choi, K. M.; Jeong, H. M.; Park, J. H.; Zhang, Y.-B.; Kang, J. K.; Yaghi, O. M. Supercapacitors of Nanocrystalline Metal-Organic Frameworks. *ACS Nano* **2014**, *8* (7), 7451–7457.

(48) Cravillon, J.; Nayuk, R.; Springer, S.; Feldhoff, A.; Huber, K.; Wiebcke, M. Controlling Zeolitic Imidazolate Framework Nano-and Microcrystal Formation: Insight into Crystal Growth by Time-Resolved in Situ Static Light Scattering. *Chem. Mater.* **2011**, *23* (8), 2130–2141.

(49) Wee, L. H.; Lohe, M. R.; Janssens, N.; Kaskel, S.; Martens, J. A. Fine Tuning of the Metal-Organic Framework Cu 3 (Btc) 2 Hkust-1 Crystal Size in the 100 Nm to 5 Micron Range. *J. Mater. Chem.* **2012**, *22* (27), 13742–13746.

(50) Khan, N. A.; Jhung, S. H. Synthesis of Metal-Organic Frameworks (Mofs) with Microwave or Ultrasound: Rapid Reaction, Phase-Selectivity, and Size Reduction. *Coord. Chem. Rev.* **2015**, *285*, 11–23.

(51) Rieter, W. J.; Taylor, K. M. L.; An, H.; Lin, W.; Lin, W. Nanoscale Metal-Organic Frameworks as Potential Multimodal Contrast Enhancing Agents. *J. Am. Chem. Soc.* **2006**, *128* (28), 9024–9025.

(52) Qiu, L.-G.; Xu, T.; Li, Z.-Q.; Wang, W.; Wu, Y.; Jiang, X.; Tian, X.-Y.; Zhang, L.-D. Hierarchically Micro- and Mesoporous Metal-Organic Frameworks with Tunable Porosity. *Angew. Chem., Int. Ed.* **2008**, *47* (49), 9487–9491.

(53) Diring, S.; Furukawa, S.; Takashima, Y.; Tsuruoka, T.; Kitagawa, S. Controlled Multiscale Synthesis of Porous Coordination Polymer in Nano/Micro Regimes. *Chem. Mater.* **2010**, *22* (16), 4531−4538.

(54) Bai, Y.; Dou, Y.; Xie, L.-H.; Rutledge, W.; Li, J.-R.; Zhou, H.-C. Zr-Based Metal-Organic Frameworks: Design, Synthesis, Structure, and Applications. *Chem. Soc. Rev.* **2016**, *45* (8), 2327−2367.

(55) Xu, H.-Q.; Wang, K.; Ding, M.; Feng, D.; Jiang, H.-L.; Zhou, H.-C. Seed-Mediated Synthesis of Metal-Organic Frameworks. *J. Am. Chem. Soc.* **2016**, *138* (16), 5316−5320.

(56) Li, P.; Klet, R. C.; Moon, S.-Y.; Wang, T. C.; Deria, P.; Peters, A. W.; Klahr, B. M.; Park, H.-J.; Al-Juaid, S. S.; Hupp, J. T.; Farha, O. K. Synthesis of Nanocrystals of Zr-Based Metal−Organic Frameworks with Csq-Net: Significant Enhancement in the Degradation of a Nerve Agent Simulant. *Chem. Commun.* **2015**, *51* (54), 10925−10928.

(57) Yaghi, O. M.; O'Keeffe, M.; Ockwig, N. W.; Chae, H. K.; Eddaoudi, M.; Kim, J. Reticular Synthesis and the Design of New Materials. *Nature* **2003**, *423* (6941), 705−714.

(58) Wang, T. C.; Bury, W.; Gómez-Gualdrón, D. A.; Vermeulen, N. A.; Mondloch, J. E.; Deria, P.; Zhang, K.; Moghadam, P. Z.; Sarjeant, A. A.; Snurr, R. Q.; Stoddart, J. F.; Hupp, J. T.; Farha, O. K. Ultrahigh Surface Area Zirconium Mofs and Insights into the Applicability of the Bet Theory. *J. Am. Chem. Soc.* **2015**, *137* (10), 3585−3591.

(59) Kalidindi, S. B.; Nayak, S.; Briggs, M. E.; Jansat, S.; Katsoulidis, A. P.; Miller, G. J.; Warren, J. E.; Antypov, D.; Corà, F.; Slater, B.; et al. Chemical and Structural Stability of Zirconium-Based Metal-Organic Frameworks with Large Three-Dimensional Pores by Linker Engineering. *Angew. Chem.* **2015**, *127* (1), 223−228.

(60) Gomez-Gualdron, D. A.; Gutov, O. V.; Krungleviciute, V.; Borah, B.; Mondloch, J. E.; Hupp, J. T.; Yildirim, T.; Farha, O. K.; Snurr, R. Q. Computational Design of Metal−Organic Frameworks Based on Stable Zirconium Building Units for Storage and Delivery of Methane. *Chem. Mater.* **2014**, *26* (19), 5632−5639.

(61) Deria, P.; Gómez-Gualdrón, D. A.; Bury, W.; Schaef, H. T.; Wang, T. C.; Thallapally, P. K.; Sarjeant, A. A.; Snurr, R. Q.; Hupp, J. T.; Farha, O. K. Ultraporous, Water Stable, and Breathing Zirconium-Based Metal-Organic Frameworks with Ftw Topology. *J. Am. Chem. Soc.* **2015**, *137* (40), 13183−13190.

(62) Farha, O. K.; Hupp, J. T. Rational Design, Synthesis, Purification, and Activation of Metal-Organic Framework Materials. *Acc. Chem. Res.* **2010**, *43* (8), 1166−1175.

(63) Gomez-Gualdron, D. A.; Moghadam, P. Z.; Hupp, J. T.; Farha, O. K.; Snurr, R. Q. Application of Consistency Criteria to Calculate Bet Areas of Micro- and Mesoporous Metal-Organic Frameworks. *J. Am. Chem. Soc.* **2016**, *138* (1), 215−224.

(64) Liu, Y.; Moon, S.-Y.; Hupp, J. T.; Farha, O. K. Dual-Function Metal-Organic Framework as a Versatile Catalyst for Detoxifying Chemical Warfare Agent Simulants. *ACS Nano* **2015**, *9* (12), 12358−12364.

(65) Schneider, C. A.; Rasband, W. S.; Eliceiri, K. W. Nih Image to Imagej: 25 Years of Image Analysis. *Nat. Methods* **2012**, *9* (7), 671−675.

(66) Mondloch, J. E.; Katz, M. J.; Isley Iii, W. C.; Ghosh, P.; Liao, P.; Bury, W.; Wagner, G. W.; Hall, M. G.; DeCoste, J. B.; Peterson, G. W.; Snurr, R. Q.; Cramer, C. J.; Hupp, J. T.; Farha, O. K. Destruction of Chemical Warfare Agents Using Metal−Organic Frameworks. *Nat. Mater.* **2015**, *14* (5), 512−516.

(67) Waugh, A.; Grant, A. *Ross & Wilson Anatomy and Physiology in Health and Illness*; Elsevier Health Sciences: Amsterdam, 2014.

(68) He, Y.; Zhang, Z.; Xiang, S.; Fronczek, F. R.; Krishna, R.; Chen, B. A Robust Doubly Interpenetrated Metal-Organic Framework Constructed from a Novel Aromatic Tricarboxylate for Highly Selective Separation of Small Hydrocarbons. *Chem. Commun.* **2012**, *48* (52), 6493−6495.